Journal of Electron Spectroscopy and Related Phenomena 258 (2022) 147221

Contents lists available at ScienceDirect

Journal of Electron Spectroscopy and Related Phenomena

journal homepage: www.elsevier.com/locate/elspec

Ultrafast X-ray photoelectron diffraction from free molecules: Simulations of diffraction profiles from transient intermediates in the elimination reaction of $C_2H_4I_2$

S. Minemoto [a], J.H. Mun [b], T. Teramoto [c], A. Yagishita [d,*], S. Tsuru [e]

[a] Department of Physics, Graduate School of Science, The University of Tokyo, 7-3-1 Hongo, Bunkyo-ku, Tokyo 113-0033, Japan
[b] Center for Attosecond Science and Technology, Max Planck POSTECH/KOREA Research Initiative, 77 Cheongam-Ro, Nam-gu, Pohang, Gyeongbuk 37363, Republic of Korea
[c] Institute for Radiation Sciences, Osaka University, 1-1 Machikaneyama-cho, Toyonaka, Osaka 560-0043, Japan
[d] Photon Factory, Institute of Materials Structure Science, KEK, 1-1 Oho, Tsukuba, Ibaraki 305-0801, Japan
[e] Lehrstuhl für Theoretische Chemie, Ruhr-Universität Bochum, D-44780 Bochum, Germany

ARTICLE INFO

Keywords:
Ultrafast X-ray photoelectron diffraction
Soft X-ray free-electron laser
Velocity-map imaging spectrometer
C 1*s* XPD profiles
Transient structures
Bridged-form C_2H_4I intermediate

ABSTRACT

We have performed the simulations of *C* 1 *s* X-ray photoelectron diffraction (XPD) profiles from $C_2H_4I_2$, bridged and classical anti-forms of C_2H_4I intermediates and C_2H_4 products to capture structures of transient intermediates in the elimination reaction of $C_2H_4I_2$, under our ultrafast X-ray photoelectron diffraction (UXPD) scheme for free molecules using soft X-ray free-electron laser (SXFEL). In the UXPD scheme, the sample molecules are aligned in advance by near-infrared (NIR) laser with ns pulse duration before applying a pump — probe method. Then, we have considered alignment control of $C_2H_4I_2$ by using the elliptically polarized NIR laser to realize the UXPD experiments for the free molecules. As the results of simulations of XPD profiles from the laser-aligned $C_2H_4I_2$ molecules, we have demonstrated the two-dimensional (2D) color maps of the *C* 1 *s* XPD profiles from $C_2H_4I_2$, C_2H_4I, and C_2H_4. The 2D color maps have revealed that the transient *C* 1 *s* XPD profiles from the bridged-form and classical anti-form C_2H_4I intermediates exhibit remarkable differences, reflecting different intra-molecular scattering pathways of *C* 1 *s* photoelectrons within the intermediates. Thus, the present result has proved that UXPD for the free molecules has an advantage, compared with other traditional diffraction methods.

1. Introduction

Photoelectron angular distributions (PADs) from free molecules have been measured for an increasing variety of purposes, including examining details of electron correlation and photoemission dynamics, demonstrating electron diffraction as a structural probe of single molecules, and probing time-resolved photochemical reactions [1–5] and references therein. Among such PAD studies, we found that molecular frame photoelectron angular distributions (MFPADs) for the inner-shell photoelectrons, with energy of > 100 eV, are less influenced by details of molecular potential; thus, the MFPADs are well described by X-ray photoelectron diffraction (XPD) picture [6]. Theoretically, photoelectron diffraction is a consequence of interference between a directly emitted photoelectron wave and elastically scattered waves by surrounding atoms. Thus, the MFPAD or XPD profiles might provide a mean of determining molecular structure in an element-specific fashion. In fact, surface structural analyses based on the XPD theory have been widely developed [7–11]. Moreover, several methodologies for the structural analyses have been applied, such as trial-and-error method [12], real-space triangular method [13], and holography [14]. The latter two methods, in which an XPD profile in momentum space is inversely transformed into an atomic position map in real space *via* Fourier transform with some corrections and modifications, are not applicable to the XPD profiles from the free molecules. This inapplicability is because the scattering amplitudes are not isotropic and phase-shifts of them are strongly dependent on scattering processes. Hence, we adopted the trial-and-error method to determine molecular structures of static ground state molecules from our experimental XPD profiles [15]. Then, our method confirmed that bond lengths and bond angles can be determined with a resolution of less than 0.1 Å and 10°, respectively. Therefore, on the basis of these achievements, we proposed an ultrafast XPD (UXPD) scheme using soft X-ray free-electron lasers (SXFELs) to

* Corresponding author.
E-mail address: akira.yagishita@kek.jp (A. Yagishita).

https://doi.org/10.1016/j.elspec.2022.147221
Received 16 February 2022; Received in revised form 24 June 2022; Accepted 24 June 2022
Available online 3 July 2022
0368-2048/© 2022 Elsevier B.V. All rights reserved.

observe experimentally ultrafast photochemical reactions [5,15]. Meanwhile, several other methods have been proposed or demonstrated, including ultrafast X-ray diffraction (UXD) using the recently developed femtosecond X-ray free-electron lasers (XFELs), ultrafast electron diffraction (UED) using short pulses of electron beams, and laser-induced electron diffraction (LIED) using recollision electrons that have tunneled out previously from the target [16–19].

Time-resolved electron and X-ray diffraction are the two principal experimental probes for transient molecular structure determination. Moreover, the UXPD has been suggested as a promising probe by a few research teams including ours, for having the element-specific fashion. Therefore, several proposals [5,15,20–23] and test experiments [24–29] for the UXPD have been published. However, results on the transient structure of molecules during chemical reactions have not been reported yet except for the recent paper [30] on the breakup process of O_2 molecules, applying SXFEL pump – SXFEL probe measurements. The ultrafast dynamics of O_2 molecules have been revealed through both triple coincidence and high-repetition SXFEL pulse capabilities [30]. However, triple coincidence rates are extremely low compared with single photoelectron detection rates, and processing of triple coincidence data is cumbersome compared with direct measuring of single photoelectron momentum image. Therefore, our UXPD scheme for the free molecules consists of four steps; (1) near-infrared (NIR) laser with ns pulse duration aligns sample molecules, (2) optical laser with fs pulse duration pumps the aligned sample molecules, (3) SXFEL with fs pulse duration probes the molecules by measuring two-dimensional (2D) XPD images with velocity-map imaging spectrometer (VMI) [27–29] as a function of delay time between the pump and probe pulses, and (4) the transient molecular structures are determined by applying the trial-and-error method to the measured XPD images.

In this Article, we report the simulation results on *C* 1 *s* XPD profiles to capture structures of transient intermediates in the elimination reaction of 1, 2-diiodoethane ($C_2H_4I_2$) molecules, which will be obtainable with our UXPD experiment. In the simulations, the photon energy of 410 eV for SXFEL was selected, *i.e.*, *C* 1 *s* photoelectron energy was set to 120 eV. From experimental point of view, the use of such SXFEL has the following benefits: The photoionization cross sections for soft X-rays < 1 keV are two-orders of magnitudes larger than those of for X-ray > 4 keV [31] and the band pass of SXFEL is one-order of magnitudes smaller than that of XFEL. The *C* 1 *s* XPD profiles for the laser-aligned $C_2H_4I_2$ molecules were obtained by the density functional theory (DFT) calculations. To mimic time-resolved UXD for transient intermediates of $C_2H_4I_2$ in solution in Ref. [32], we calculated the *C* 1 *s* XPD profiles for the ground state $C_2H_4I_2$, the bridged and classical (non-bridged) C_2H_4I radical intermediates, and the C_2H_4 product.

2. Experimental scheme

Fig. 1 shows the schematic of the experimental setup for our UXPD scheme for the free molecules. We introduce three kind of laser beams into VMI, *i.e.*, nanosecond Nd:YAG laser ($\lambda = 1064$ nm) for molecular alignment, femtosecond ultraviolet (UV) laser ($\lambda = 267$ nm, ~ 50 fs, 10 μJ) for exciting the aligned molecules, and femtosecond SXFEL laser ($\lambda = 3.0$ nm, ~ 50 fs, ~ 100 μJ) for the probe. The cylindrically symmetric axis of the VMI spectrometer is placed along the *y* axis, and the three laser beams propagate coaxially along the *x* axis. The polarization vectors of both the Nd:YAG and UV laser beams are controllable on the *yz* plane.

The Nd:YAG laser pulses, with the energy of ~ 700 mJ/pulse and duration of ~ 10 ns, are focused by a plano-convex lens into the interaction region of our diffractometer comprising the VMI spectrometer [27,28]. The ellipticity of the Nd:YAG laser polarization is controlled by the combination of $\lambda/2$ and $\lambda/4$ waveplates. For the UXPD, the C—C axis in $C_2H_4I_2$ is preferentially aligned along the *y* axis. To realize this, the major axis of the polarization ellipse of the Nd:YAG laser is rotated by 43° clockwise with respect to the *z* axis, and the ellipticity is set to be ~ 0.9, as discussed in Section 3. By focusing to the spot sizes of ~ 60 μm, the total intensity, the sum of major and minor components, of $\sim 2.5 \times 10^{12}$ W/cm^2 is available at the focus.

The output of the Ti:saphire amplifier is frequency up-converted to 267 nm by the third order harmonics generation process using β-BBO crystals, and guided to the VMI chamber collinearly with the Nd:YAG laser beam. In $C_2H_4I_2$, the dominant transition due to a 267 nm photon originates from promotion of an electron from a non-bonding (n) iodine orbital to an anti-bonding (σ *) orbital localized on the C–I bond. Under the condition of output energy of ~ 10 μJ/pulse, one can estimate that

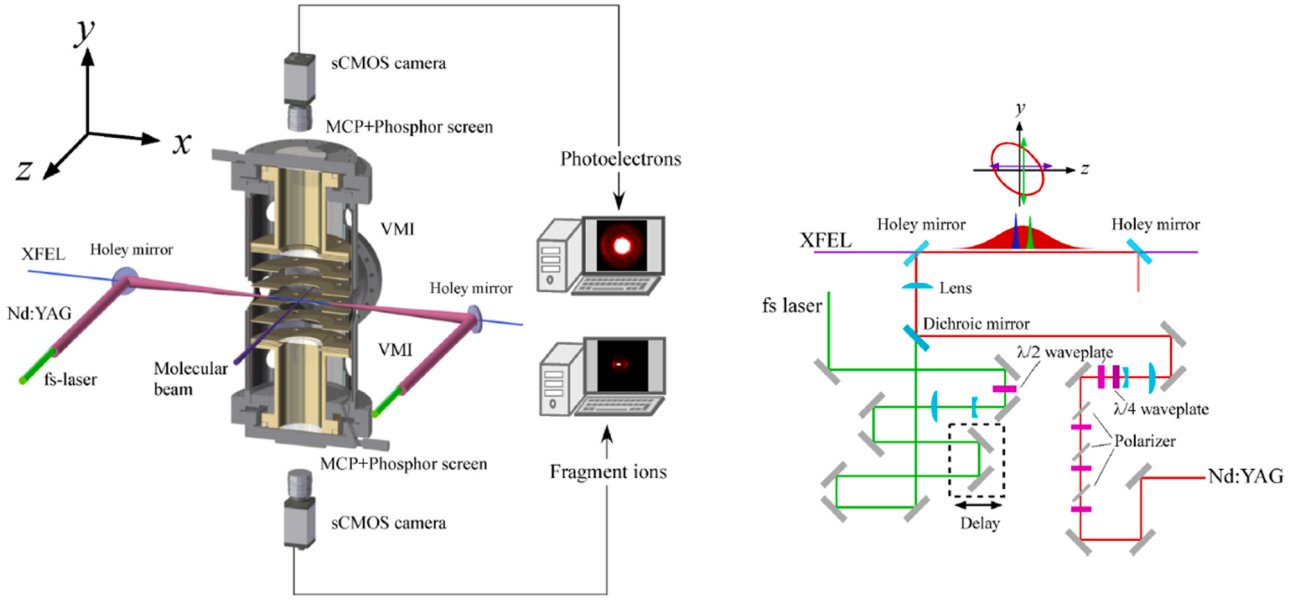


Fig. 1. Schematic of the experimental setup (left) and optical paths of alignment, pump, and probe lasers (right). Laser beams propagating along the *x* axis in a collinear arrangement intersect a supersonic pulsed molecular beam along the *z* axis at the center of a vacuum chamber. The polarizations of the Nd:YAG and fs-lasers are controlled by $\lambda/2$ and $\lambda/4$ waveplates. The Nd:YAG laser is used to align the sample molecules, which are excited by fs-laser and are probed by the SXFEL. 2D XPD images are recorded by the upper VMI. 2D images of the fragment ions are registered by the lower VMI.

more than 30% of the sample molecular ensemble are excited, referring to the relevant cross sections of 5×10^{-18} cm^2 [33]. To match the focus points of both the Nd:YAG and UV laser beams, the divergence of the UV laser is tuned by adjusting the telescope inserted in the beam path. The linear polarization vector of the UV laser is set to be parallel to the *y* axis by a λ/2 waveplate. The spatial overlap of both the UV and Nd:YAG beams are confirmed outside the vacuum chamber by picking up a small portion of the beams by a beam sampler.

SXFEL pulses, with the typical energy of ~ 100 μJ/pulse and duration of ~ 50 fs, are focused to the interaction region by a K-B mirror in a beamline. The typical bandwidth of the SXFEL is ~ 0.5%, *i.e.*, ~ 2 eV at the photon energy of 410 eV. The polarization vector of the SXFEL is fixed along the *z* axis direction. The Nd:YAG and UV laser beams are merged collinearly with the SXFEL by a holey mirror inside the vacuum chamber. The spatial overlap of the SXFEL, Nd:YAG, and UV laser beams is first examined by monitoring images on a Ce:YAG phosphor screen at the interaction region, and then confirmed by monitoring the degree of alignment of the sample molecules. The temporal overlap between the SXFEL and Nd:YAG laser pulses is monitored using a fast photodiode. The temporal overlap between the SXFEL and UV laser is first checked by using a fast photodiode and then confirmed by measuring $C\ 1s$ photoelectron sidebands due to two-color above-threshold ionization [34].

A pulsed supersonic molecular beam is formed by expanding a gas mixture of the sample molecules diluted in 40 bar helium through a pulsed valve, which is developed by Even and Lavie [35], into the vacuum chamber. In order to obtain sufficient signal intensities, the pulsed valve needs to be heated to provide a partial pressure of ~ 1 kPa for the sample molecules. An adequate temperature of the valve is estimated to be ~ 90 °C. The molecular beam passes through a 3 mmϕ skimmer and is introduced into the interaction region where the three lasers overlap.

The momenta of photoelectrons and fragment-photoions produced by the SXFEL pulses are measured by using the faced VMIs [27,28]. The velocity-focused photoelectrons are detected by a chevron-stacked dual microchannel plate (MCP) backed by a phosphor screen. The image on the phosphor screen, which is the projection of the three dimensional (3D) momentum distributions onto the *xz* plane, is recorded shot by shot using the sCMOS camera, and it is stored on the PC. The 2D photoelectron momentum images obtained with and without the sample gas are alternately measured and the objective images that originated from the residual-free sample gas are then obtained by subtracting the latter from the former. Simultaneously, the produced fragment-photoions are accelerated toward the other VMI, and they are detected by the similar system to the photoelectron measurements. The 2D momentum images of I^+ and C^+ ions are used to evaluate the degrees of alignment, $< \cos^2\theta >$and., respectively, which are defined in Section 3.

3. Control of alignment of $C_2H_4I_2$ molecules

In this section, we consider alignment control of $C_2H_4I_2$ by using elliptically polarized Nd:YAG laser, see Fig. 2. In Fig. 2(a), the molecular reference frame is defined by the Cartesian coordinate of (X_m, Y_m, Z_m), *i.e.*, the X_m axis is taken to coincide with the *x* axis of the laboratory frame, the Y_mZ_m plane with the σ_h mirror plane, and the *I*—*I* axis with the Z_m, according to Ref. [36]. The photon reference frame for the Nd:YAG laser is defined by the Cartesian coordinate of (X_p, Y_p, Z_p), in which the X_p axis is chosen to coincide with the propagation direction of the laser, the Y_p axis with the minor axis of the polarization ellipse, and the Z_p axis with the major axis of the ellipse. In Fig. 2(b), the directions of both the X_p and X_m axis are reversed with respect to those in Fig. 2(a). It should be noted that the two alignment configurations in Fig. 2(a) and (b) must be taken into account under the alignment control using the elliptically polarized Nd:YAG laser. Namely, in this control, the rotational direction of the polarization ellipse is not imprinted into the sample molecules.

Irradiation of the NIR laser polarized linearly along the Z_p axis induces alignment of the Z_m axis of the molecule towards the Z_p axis, as shown in Fig. 3(a). However, in this condition, the Y_mZ_m plane is freely rotated around the Z_p axis. In order to fix the rotation of the Y_mZ_m plane, the use of elliptically-polarized lasers is inevitable. When an elliptically-polarized laser is irradiated to the molecules, the Y_m axis is confined to the Y_p axis without losing the alignment of the Z_m with respect to the Z_p axis, see Fig. 3(b). Thus, all the angles of θ, ϕ and χ which are defined in Fig. 3, are controllable with the elliptically polarized laser.

Under a long pulse limit for the NIR laser, which has long pulse durations in comparison to the rotational periods of molecules, the degrees of alignment of $C_2H_4I_2$ are calculated by solving a time-independent Schrödinger equation. Here we assume a rigid-rotor approximation for the ground state molecules, where all vibrational modes are frozen at the equilibrium positions. The rigid rotor Hamiltonian in a field-free condition can be described as

$$H_{rot} = AJ^2_{Z_m} + BJ^2_{Y_m} + CJ^2_{X_m}\ , \tag{1}$$

where *A*, *B*, and *C* are the rotational constants ($A \geq B \geq C$) corresponding to the Z_m, Y_m, X_m axes, respectively [36]. J_I is an *I* component of the total angular momentum operator ***J***. Considering a laser field with non-resonant frequencies, the alignment Hamiltonian can be given as [37].

$$H_{align} = -\frac{1}{2}\left[\alpha_{Z_mZ_m}E^2_{Z_m} + \alpha_{Y_mY_m}E^2_{Y_m} + \alpha_{X_mX_m}E^2_{X_m}\right] \tag{2}$$

with$\alpha_{II}$and$E_I$are polarizability and electric field components parallel to the molecular *I* axis ($I = Z_m, Y_m, X_m$), respectively. In calculations of the molecular alignment, we used the rotational constants A = 6710, B = 508, and C = 472 MHz, and the polarizability components$\alpha_{Z_mZ_m}$ =

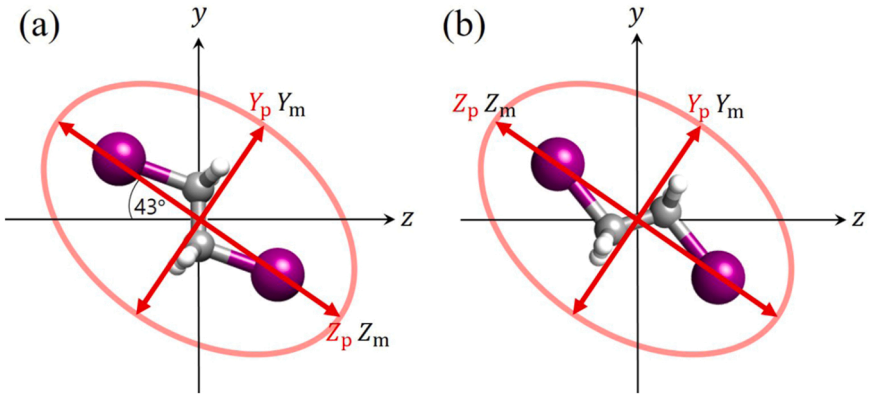


Fig. 2. Optimum alignment of a $C_2H_4I_2$ molecule by an elliptically polarized laser. (a) seen from the behind of the propagation direction of the laser and (b) seen from the front of the propagation. The polarization ellipse is tilted relative to the *z* axis, to align the C—C bond in $C_2H_4I_2$ along the *y* axis in (a).

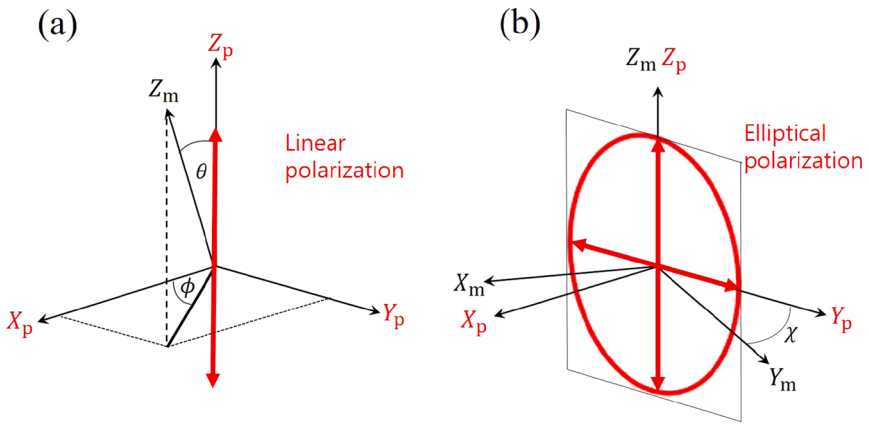


Fig. 3. Relation between molecular and photon reference frames. (a) for linear polarization and (b) for elliptical polarization. The laser propagates along the X_p axis. The polarization vector of linearly polarized laser and the major axis of elliptically polarized laser are taken to coincide with the Z_p axis. The frames are expressed by the right-hand coordinate system.

13.6, $\alpha_{Y_mY_m} = 7.5$, and $\alpha_{X_mX_m} = 3.2$ Å^3, which were calculated by using DFT of Gaussian03 program [38] with the 3–21 G basis set (It is noted that larger basis sets, *e. g.*, 6–21 G are not supported for the *I* atom even in Gaussian16 program.). Then, the total Hamiltonian for molecular rotational motions is described by the sum of Eqs. (1) and (2). The degrees of alignment calculated by numerical solutions of the Schrödinger equation for the total Hamiltonian are shown in Fig. 4. For the linear polarization, Fig. 4(a) shows the degrees of alignment,$< \cos^2\theta >$, of the Z_m axis along the Z_p, and that,$< \sin^2\theta\cos^2\phi >$, of the Z_m axis along the X_p. The degree of alignment,$< \cos^2\chi >$, of the Y_m along the Y_p, which is related to the rotation of the molecular σ_h mirror plane, is also shown. As the laser intensity increases, $< \cos^2\theta >$increases and $< \sin^2\theta\cos^2\phi >$ decreases. At the intensity of 1×10^{10} W/cm^2, $< \cos^2\theta >$reaches up to 0.95 and $< \sin^2\theta\cos^2\phi >$ down to 0.05, which means that the direction connecting *I*—*I* atoms in the $C_2H_4I_2$ molecule, the Z_m axis, is tightly aligned to the polarization direction, the Z_p axis, of the laser field. The probability of the axis distributions in θ space is shown in Fig. 4(b). On 99% of the molecular ensemble, the Z_m axes are distributed in the range of $0 \le \theta \le 0.2\pi$. We note again that, with the linear polarization, the rotation around the Z_m axis is fully random, as can be confirmed by $< \cos^2\chi > = \int \cos^2\chi d\chi / \int d\chi = 0.5$ ..

For the elliptical polarization, the rotation around the Z_m axis can be controlled, whereas the distribution of it is slightly broadened. The Y_m axis, which has the second strongest polarizability component of $\alpha_{Y_mY_m} = 7.5$, can be aligned to the direction of the Y_p axis of the polarization ellipse as shown in Fig. 3(b). Fig. 4(c) shows the degrees of alignment, $< \cos^2\theta >$, $< \sin^2\theta\cos^2\phi >$, and $< \cos^2\chi >$ as a function of the ellipticity$(= E_{Y_p}/E_{Z_p})$at the laser intensity of 2×10^{10} W/cm^2. Though $<$

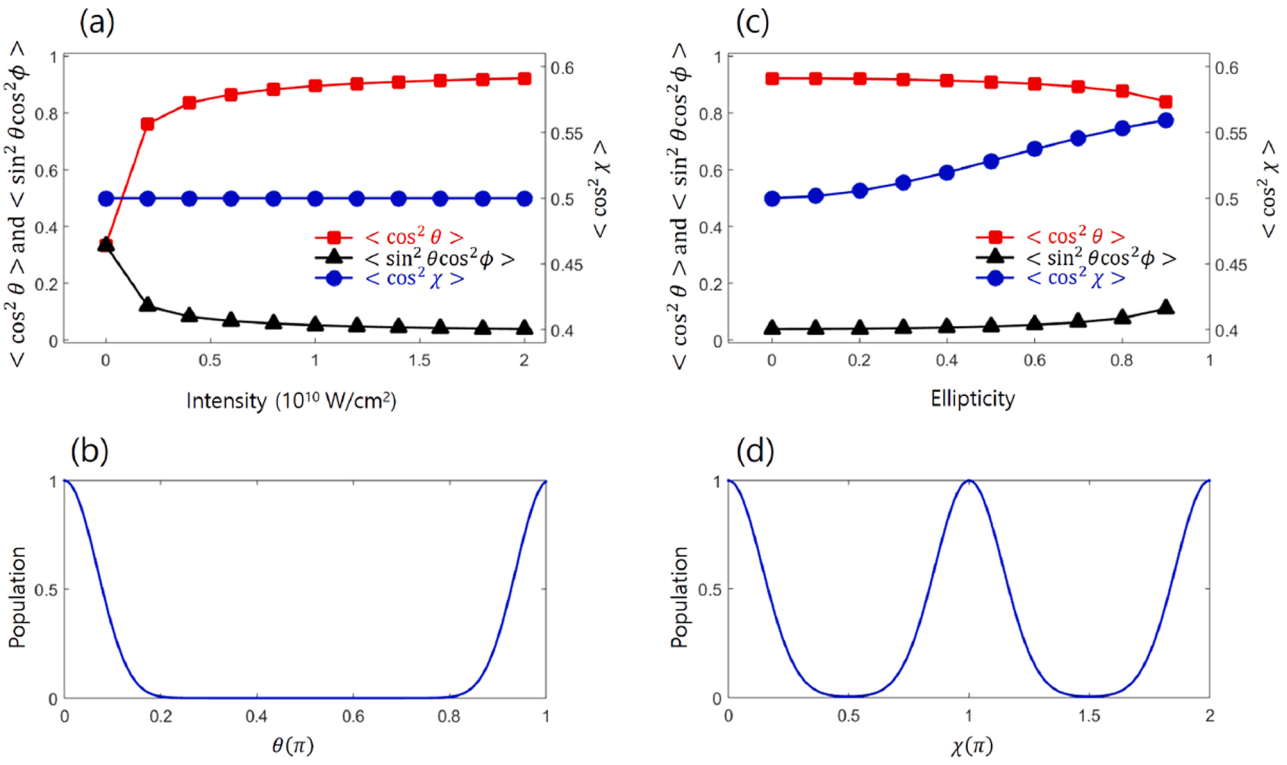


Fig. 4. Degrees of alignment and distributions of molecular axis. (a) degrees of alignment for linear polarization, (b) distributions of the Z_m axis at the intensity of 2×10^{10} W/cm^2, (c) degrees of alignment for elliptical polarization, and (d) distributions of the Y_m axis at the ellipticity of 0.9 and the intensity of 2×10^{10} W/cm^2.

$\cos^2\theta >$ ($< \sin^2\theta\cos^2\phi >$) is gradually decreased (increased) as the ellipticity increases, it still remains ~ 0.84 (~ 0.10) at the ellipticity of 0.9. At the same time, $< \cos^2\chi >$increases as the ellipticity increases. This indicates that the molecular Y_mZ_m plane is confined on the Y_pZ_p plane. At the intensity of 2×10^{10} W/cm^2 and the ellipticity of 0.9, $< \cos^2\chi >$reaches up to 0.56. In this condition, the probability of the rotational distributions of the Y_mZ_m plane in χ space is shown in Fig. 4 (d). On 82% of the molecular ensemble, the Y_m axes are distributed in the range of $-\ 0.2 \leq \chi \leq 0.2\pi$. This means that on 41% of the molecular ensemble, the C—C axes align in the range between — 0.2 and 0.2π, relative to the *y* axis as shown in Fig. 2(a). On the same amount of the molecular ensemble, the C—C axes align in the range between —0.14 and 0.26π, relative to the *z* axis as shown in Fig. 2(b). That is, the two configurations in Fig. 2(a) and (b) are involved with the equal populations in the sample molecular ensemble under the present alignment control, because the rapid oscillation of the electric fields are averaged over the long laser pulse duration in considering the molecular alignment [37].

4. Simulations of *C*1*s* XPD profiles from transient intermediates in the elimination reaction of $C_2H_4I_2$

Elimination processes of iodine atoms from $C_2F_4I_2$ and $C_2H_4I_2$ molecules pumped by the 267 nm UV laser have been intensively investigated as prototypes of stereochemical control [32,39–46]. After the excitation, the $C_2F_4I_2$ molecule in the gas phase undergoes the first elimination of an iodine atom in 200 fs, and generates an additional iodine atom and a C_2F_4 product in 25 ps, according to the mass spectrometric study [39]. The UED experiments have proved that the C_2F_4I intermediate of the elimination reaction in the gas phase has the classical (non-bridged) form, where the remaining iodine atom has a covalent bond with only one carbon atom [40–42]. The nuclear wave packet dynamics, during and after the first elimination, was investigated by combination of the UED experiments with nuclear dynamics simulations in femtosecond timescale [42]. Further, the UXD experiments have revealed that the C_2F_4I intermediate takes the classical form in the elimination reactions of $C_2F_4I_2$ dissolved in methanol [43] and cyclohexane [44]. In contrast to $C_2F_4I_2$, the UXD experiments have revealed that the form of the C_2H_4I intermediate left after the first elimination takes the bridged structure in solution, where the remaining iodine atom has two equivalent covalent bonds with the two carbon atoms. But the second elimination processes in methanol [32] and cyclohexane [45] take different paths. Ab initio and DFT calculations have indicated that the bridged structure of the C_2H_4I intermediate is plausible in the gas phase [46]. However, this prediction has not been confirmed experimentally yet.

The excited diabatic ^1B_u ($^1A'$) state in $C_2H_4I_2$ is induced by the 267 nm UV laser, according to Ref. [46]. This excitation is due to promotion of an electron from a non-bonding (n) iodine orbital to an anti-bonding (σ *) orbital localized on the C–I bond, see Fig. 5. The n → σ * excitation in $C_2F_4I_2$ has the similar character with that in $C_2H_4I_2$, where the first elimination with time constant of 200 fs is caused by the locally reduced stability on the C—I bond [42]. From this, the first elimination of an iodine atom from the $C_2H_4I_2$ molecule is also expected to occur in similar timescale. Meanwhile, alignment of $C_2H_4I_2$ molecules can be kept for 2.6 ± 1.2 ps [47]. Thus, the UXPD method proposed by us may be able to visualize the structure of the C_2H_4I intermediate during the elimination reaction of $C_2H_4I_2$ in the gas phase.

In the gas phase, 88% of $C_2H_4I_2$ takes the anti-form and remaining 12% takes the gauche-form [48]. Therefore, we consider the anti-form in the following discussions. To get structural information of the intermediates during the elimination reaction from the *C* 1 *s* UXPD images, the C—I bond direction being nearby the *z* axis is preferable. Thus, the C—C bond direction of $C_2H_4I_2$ is set to be parallel to the *y* axis in the present simulations, see Fig. 2(a). Then, the polarization vector of the pump UV laser is set to be along the *y* axis. Here, it should be noted that the two configurations depicted in Fig. 2(a) and (b) must be considered under the alignment control by using the Nd:YAG laser, as mentioned in Section 3. For the former objective configuration, the angle between the polarization vector and normal to the C—I bond is 20°, see Fig. 5(a), but for the latter non-objective, the angle is 52°, see Fig. 5(b). Taking the perpendicular transition character of the n → σ * transition into account, the ratio of contributions of the two configurations to the XPD profiles is estimated as$\cos^2 20^\circ : \cos^2 52^\circ \approx 2.3 : 1$, in the pump – probe experiments. Thus, the contribution of the non-objective configuration in Fig. 2(b) is neglected in the following simulations for simplicity. Moreover, we fixed $C_2H_4I_2$ molecule at the most probable directions under the alignment control described in Section 3, which is depicted in Fig. 6 (a). It should be mentioned that a higher degree of alignment than 0.8 is demanded to extract the molecular structures from observed XPD patterns, see our recent work in Ref. [29]. The C—C bond direction is assumed to be fixed during the first elimination process, considering the time constant, configuration character of the excited state, and the nuclear wave packet investigation in Ref. [42]. The molecular structures of $C_2H_4I_2$, the bridged and classical anti-forms of the C_2H_4I intermediates are taken from Tables 2 S, 4 S(a) and (b) of the Supporting Information in Ref. [46], respectively. The molecular structure of C_2H_4 is taken from the experimental data in Ref. [49]. The XPD profiles were calculated with the functional form of MFPAD [50,51] at the DFT/LB94 [52] level. The computations with a basis set of multicenter B-spline functions centered on all the nuclei [53,54] were performed by utilizing DTU Computing Center resources [55]. The calculated XPD profiles are incoherent superposition of those from the two degenerate *C* 1 *s* orbitals ($11a_g$ and $11b_u$ of $C_2H_4I_2$, $8a_1$ and $4b_2$ of the bridged-form of C_2H_4I, 11*a* and 12*a* of the classical anti-form of C_2H_4I, $1a_g$ and $1b_{1u}$ of C_2H_4).

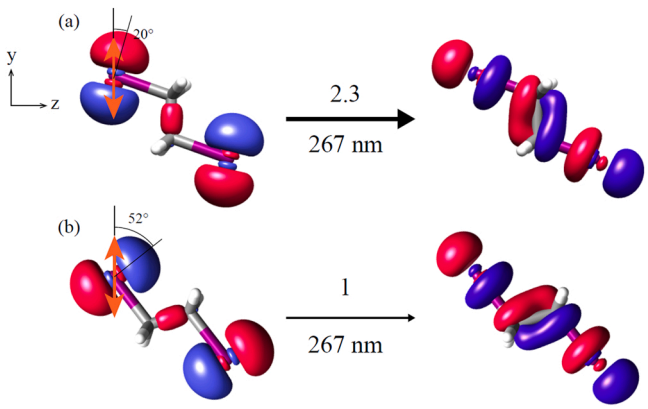


Fig. 5. Dominant components of the natural transition orbitals of the excitation with the 267 nm laser for the two configurations. (a) objective configuration in Fig. 2(a) and (b) non-objective configuration in Fig. 2(b). Molecular geometry is taken from Table 2S of the Supporting Information in Ref. [46]. Numbers above the arrows indicate relative probabilities of the excitation, which are estimated from the angle between the polarization direction of the laser and the transition dipole.

In the present simulations, the XPD profiles were calculated for the two candidate reaction paths, see Fig. 6(a):

$$C_2H_4I_2(\text{anti-form}) \xrightarrow{h\nu(267\text{nm})} C_2H_4I(\textit{bridged or classical}) + I \rightarrow C_2H_4 + 2I \quad (3)$$

Fig. 6(b) shows the 2D color maps of the *C* 1*s* XPD profiles from $C_2H_4I_2$, the bridged and classical anti-forms of C_2H_4I, and C_2H_4, which were calculated at the photoelectron energy of 120 eV. The 2D color maps are the projection of 3D *C* 1*s* MFPAD on the *xz* plane, which are measurable by using our VMI system. The first dissociation may occur at two sites of the C—I bonds with an equal probability, so that the two

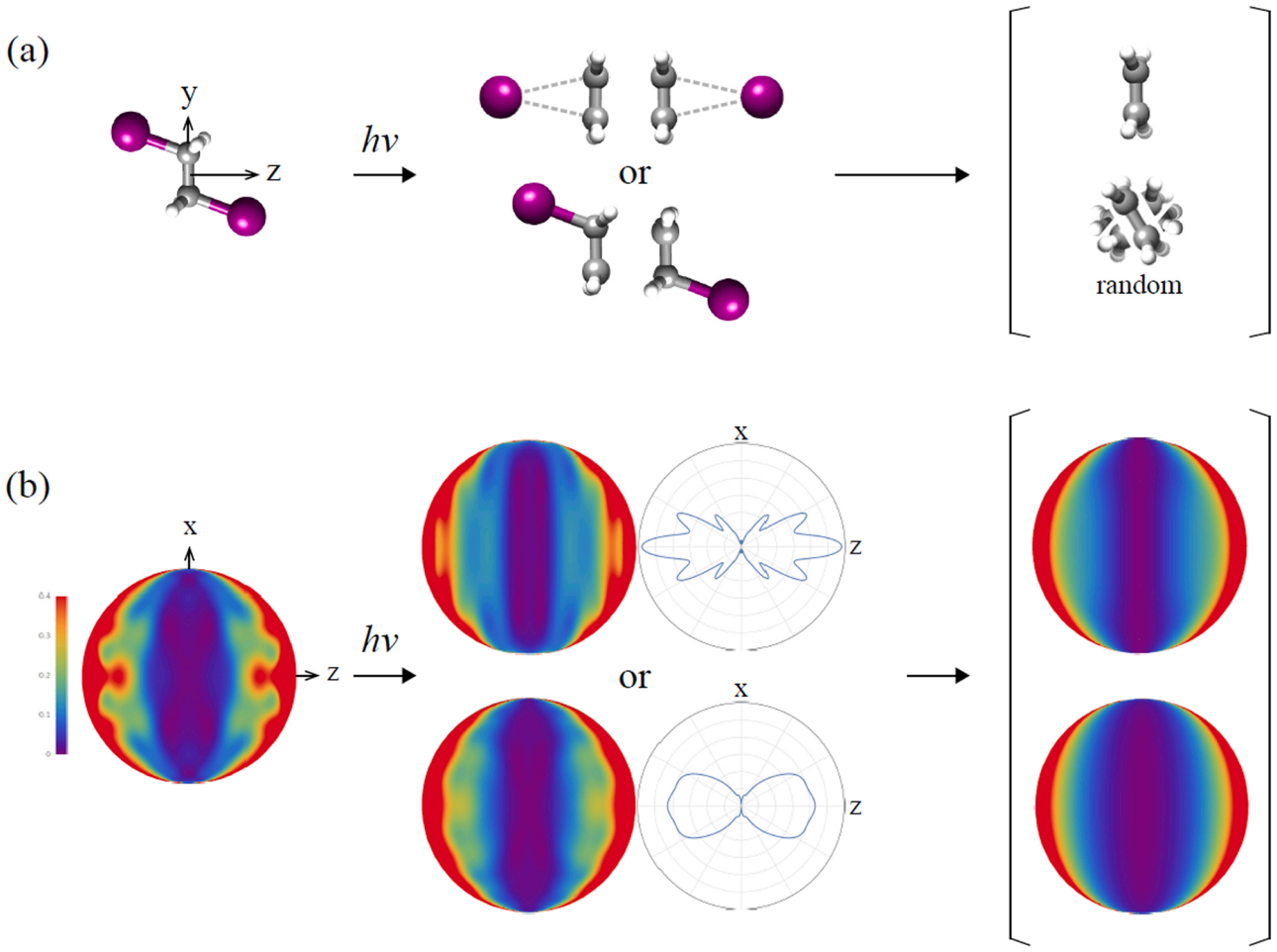


Fig. 6. Reaction paths from $C_2H_4I_2$ (upper) and transient XPD profiles (lower). In (a), two possible intermediates and aligned and randomly oriented C_2H_4 are shown. In (b), XPD profiles, from $C_2H_4I_2$ (left), bridged-form (upper middle) and anti-form (lower middle) of the C_2H_4I radical intermediate, and C_2H_4 product (right), are shown by 2D color maps. On the bridged-form (upper middle) and anti-form (lower middle), polar plots are shown as well, to demonstrate interferences caused by intra-molecule scattering of photoelectrons. 3D *C1s* MFPADs were calculated at the photoelectron energy of 120 eV and then XPD profiles were obtained by the projection of the 3D MFPADs on the *xz* plane. The σ_h plane of the $C_2H_4I_2$ molecule was put on the *yz* plane and the C—C bond was fixed parallel to the *y* axis throughout the elimination reactions. The XPD profile in the lower right position is from randomly oriented C_2H_4 molecules, which is expressed by the asymmetry parameter β=1.87.

configurations for one intermediate shown in the figure equally contribute to the XPD profiles. In the 2D color map from $C_2H_4I_2$, interference effects between the waves scattered by the two iodine atoms are observed at the polar angle $\theta \sim 30^\circ$ in the periphery of the map, and more obviously around the points of ($z \sim \pm 0.7 \times |z_{max}|$, $x = 0$), see left in Fig. 6(b). In the classical anti-form C_2H_4I intermediate, the difference of ∠CCI from $C_2H_4I_2$ is less than 2°. Thus, in the 2D map from C_2H_4I, overall XPD profile is similar with that from $C_2H_4I_2$, but the fine structure due to the interferences, which are observed in the 2D map from $C_2H_4I_2$, disappears, see left and lower middle in Fig. 6(b). After this, the XPD profile varies from the classical anti-form C_2H_4I to the aligned C_2H_4, see lower middle and upper right in Fig. 6(b). Here, it is noted that the XPD profile from the aligned C_2H_4 is similar with that from the randomly oriented C_2H_4, see lower and upper right in Fig. 6(b). That is, on one hand, the XPD profile projected on the *xz* plane is insensitive to the C—C direction of C_2H_4 perpendicular to the polarization vector (the z axis), which is expressed by the PAD ($\cos^2\theta$) for $s \rightarrow p$ transitions. On the other hand, PAD from the randomly oriented C_2H_4 is described by one asymmetry parameter β; $\propto 1 + \beta P_2(\cos\theta)$. Thus, for $\beta > \sim 1.5$, the two PAD's are similar each other. However, we can say that the XPD profile from the randomly oriented C_2H_4 is rather realistic prediction in the longer time than 2.6 ± 1.2 ps, because the molecular alignment decays with a time constant of 2.6 ± 1.2 ps [47]. In contrast to the above discussion, the XPD profile from the bridged-form C_2H_4I intermediate exhibits enhanced scattering effects, due to drastic change of ∠CCI and incoherent superposition of the photoelectron intensities from the two carbon atoms suffering from the equivalent scattering effects, see upper middle in Fig. 6(b). This implies that the forms of the C_2H_4I intermediates could be determined by observing such drastic change of the XPD profiles, see left and upper middle in Fig. 6(b). To emphasize power of the UXPD, the one dimensional (1D) polar plots of the *C* 1 *s* XPD profiles, which are the *C* 1 *s* photoelectron intensities as a function of the polar angle θ at the r_{max} of the 2D color maps, are also shown in Fig. 6(b). One can see the remarkable differences between the polar plot for the bridged-form intermediate and that for the classical anti-form. Namely, the structures of both the bridged-form intermediate and the classical anti-form are directly reflected on the XPD profiles. This is an advantage of the UXPD, compared with other diffraction methods.

5. Summary

Several proposals and test experiments of the UXPD for the free molecules have been published as mentioned in Introduction. However, UXPD experimental results on capturing transient molecular structures during ultrafast photochemical reactions have not been reported yet. Thus, in advance of the coming experiments, we have performed the

simulations of *C* 1 *s* XPD profiles from $C_2H_4I_2$, the bridged and classical anti-forms of C_2H_4I, and C_2H_4 to capture transient structures of intermediates in the ultrafast elimination reaction of $C_2H_4I_2$. Our simulations have revealed that the *C* 1 *s* XPD profile from the bridged-form remarkably differs from that from the classical anti-form C_2H_4I intermediates, reflecting different intra-molecular scattering pathways of *C* 1 *s* photoelectrons within the intermediates. From this promising result, one can expect that one will be able to know the molecular structure of the transient intermediates in real time by watching the XPD profiles on the screen of PC, if one will successfully apply the UXPD to photochemical reactions.

Financial support

This research was supported by the Bilateral Joint Research Project (JPJSBP1 2019833) and KAKENHI No. 18K05048, JSPS. This work was partly supported by NRF Grants (NRF-2020R1C1C1012953). This research was partly funded through a Research Fellowship (JPN 1201668 HFST-P) to ST of the Alexander von Humboldt Foundation. AY acknowledges the support from IQCE Research Fellowship for Senior Fellow.

Declaration of Competing Interest

The authors declare that they have no known competing financial interests or personal relationships that could have appeared to influence the work reported in this paper.

Data Availability

Data will be made available on request.

Acknowledgements

The authors express their thanks to Prof. P. Decleva, CNR IOM and DSCF, Università degli Studi di Trieste, for his calculations of the ground-state electron densities. This research was supported by the Bilateral Joint Research Project (JPJSBP1 2019833) and KAKENHI No. 18K05048, JSPS. This work was partly supported by NRF Grants (NRF-2020R1C1C1012953). This research was partly funded through a Research Fellowship (JPN 1201668 HFST-P) to ST of the Alexander von Humboldt Foundation. AY acknowledges the support from IQCE Research Fellowship for Senior Fellow.

References

[1] A. Yagishita, K. Hosaka, J.-I. Adachi, J. Electron Spectrosc. Relat. Phenom. 142 (2005) 295–312.
[2] T. Suzuki, Int. Rev. Phys. Chem. 31 (2012) 265–318.
[3] K.L. Reid, Mol. Phys. 110 (2012) 131–147.
[4] J. Phys. B: At. Mol. Opt. Phys. 45 (2012) Special issue on molecular-frame photoelectron angular distributions.
[5] A. Yagishita, J. Electron Spectrosc. Relat. Phenom. 200 (2015) 247–256.
[6] M. Kazama, et al., J. Electron Spectrosc. Relat. Phenom. 185 (2012) 535–545.
[7] C.S. Fadley, Surf. Sci. Rep. 19 (1993) 231–264.
[8] D.P. Woodruff, A.M. Bradshaw, Rep. Prog. Phys. 57 (1994) 1029–1080.
[9] C.S. Fadley, et al., Prog. Surf. Sci. 54 (1997) 341–386.
[10] C.S. Fadley, et al., J. Phys.: Condens. Matter 13 (2001) 10517–10532.
[11] D.P. Woodruff, Surf. Sci. Rep. 62 (2007) 1–38.
[12] R. Terborg, et al., Phys. Rev. B 66 (2002), 085333-1-14.
[13] Ph Hofmann, K. –M. Schindler, Phys. Rev. B 47 (1993) 13941–13943.
[14] J.J. Barton, Phys. Rev. Lett. 61 (1988) 1356–1359.
[15] M. Kazama, et al., , Phys. Rev. A 87 (2013), 063417-1-15.
[16] T. Elsaesser, M. Woerner, J. Chem. Phys. 140 (2014), 020901-1-11.
[17] J. Xu, et al., J. Phys. B: . Mol. Opt. Phys. 49 (2016), 112001-1-17.
[18] L. Young, et al., J. Phys. B: . Mol. Opt. Phys. 51 (2018), 032003-1-45.
[19] Z. Li, et al., ACS Photonics 7 (2020) 296–320.
[20] F. Krasniqi, et al., Phys. Rev. A 81 (2010), 033411-1-11.
[21] X. Wang, et al., Sci. Rep. 6 (2016), 23655-1-11.
[22] S. Tsuru, et al., Phys. Rev. A 95 (2017), 043404-1-9.
[23] S. Tsuru, et al., J. Chem. Phys. 148 (2018), 124101-1-10.
[24] R. Boll, et al., Phys. Rev. A 88 (2013), 061402(R) -1-5.
[25] D. Rolles, et al., J. Phys. B: . Mol. Opt. Phys. 47 (2014), 124035-1-12.
[26] R. Boll, et al., Faraday Discuss. 171 (2014) 57–80.
[27] K. Nakajima, et al., Sci. Rep. 5 (2015), 14065-1-11.
[28] S. Minemoto, et al., Sci. Rep. 6 (2016), 38654-1-9.
[29] T. Teramoto, et al., Struct. Dyn. 9 (2022), 024303-1-11.
[30] G. Kastirke, et al., Phys. Rev. X 10 (2020), 021052-1-9.
[31] E.B. Saloman, J.H. Hubbell, J.H. Scofield, Data Nucl. Data Tables 38 (1988) 1–196.
[32] H. Ihee, et al., Science 309 (2005) 1223–1227.
[33] X. Zheng, et al., Chem. Phys. Lett. 292 (1998) 295–306.
[34] S. Minemoto, et al., J. Phys. B: . Mol. Opt. Phys. 51 (2018), 075601.
[35] U. Even, J. Jortner, D. Noy, N. Lavie, J. Chem. Phys. 112 (2000) 8068–8071.
[36] R.N. Zare, Angular Momentum. Understanding Spatial Aspects in Chemistry and Physics, John Wiley and Sons, New York, Chichester, Brisbane, Toronto, Singapore, 1988.
[37] M. Artamonov, T. Seideman, J. Chem. Phys. 128 (2008), 154313.
[38] M.J. Frisch et al.Gaussian03, Revision C.02 2004 Gaussian, Inc., Wallingford CT.
[39] D. Zhong, S. Ahmad, A.H. Zewail, J. Am. Chem. Soc. 119 (1997) 5978–5979.
[40] H. Ihee, V.A. Lobastov, U.M. Gomez, B.M. Goodson, R. Srinivasan, C.-Y. Ruan, A. H. Zewail, Science 291 (2000) 458–462.
[41] H. Ihee, B.M. Goodson, R. Srinivasan, V.A. Lobastov, A.H. Zewail, J. Phys. Chem. A 106 (2002) 4087–4103.
[42] K.J. Wilkin, R.M. Parrish, J. Yang, T.J.A. Wolf, J.P.F. Nunes, M. Guehr, R. Li, X. Shen, Q. Zheng, X. Wang, T.J. Martinez, M. Centurion, Phys. Rev. A 100 (2019), 023402.
[43] J.H. Lee, T.K. Kim, J. Kim, Q. Kong, M. Cammarata, M. Lorenc, M. Wulff, H. Ihee, J. Am. Chem. Soc. 130 (2008) 5834–5835.
[44] J. Gu, S. Lee, S. Eom, H. Ki, E.H. Choi, Y. Lee, S. Nozawa, S. Aadachi, J. Kim, H. Ihee, Int. J. Mol. Sci. 22 (2021) 9793.
[45] J. Kim, J.H. Lee, J. Kim, S. Jun, K.H. Kim, T.W. Kim, M. Wulff, H. Ihee, J. Phys. Chem. A 116 (2012) 2713–2722.
[46] Q. Kong, J. Kim, M. Lorenc, T.K. Kim, H. Ihee, M. Wulff, J. Phys. Chem. A 109 (2005) 10451–10458.
[47] P. Reckenthaeler, M. Centurion, W. Fuß, S.A. Trushin, F. Krausz, E.E. Fill, Phys. Rev. Lett. 102 (2009), 213001.
[48] E. Rømhen, K. Hagen, R. Stølevik, J. Tremmel, J. Mol. Struct. 243 (1991) 419–426.
[49] E. Hirota, Y. Endo, S. Saito, K. Yoshida, I. Yamaguchi, K. Machida, J. Mol. Spectrosc. 89 (1981) 223–231.
[50] N. Chandra, J. Phys. B 20 (1987) 3405–3415.
[51] M. Stener, Chem. Phys. Lett. 356 (2002) 153–160.
[52] R. van Leeuwen, E.J. Baerends, Phys. Rev. A 49 (1994) 2421–2431.
[53] E. Bachau, P. Cormier, J.E. Decleva, Hansen, F. Martín, Rep. Prog. Phys. 64 (2001) 1815–1942.
[54] D. Toffoli, M. Stener, G. Fronzoni, P. Decleva, Chem. Phys. 276 (2002) 25–43.
[55] D.T.U. Computing Center *DTU Computing Center resources* Tech. Univ. Den. 2021 doi: 10.48714/DTU.HPC.0001.